NOTE

The temperature dependence of gradient system response characteristics

Manuel Stich[1,2,4] (iD) | **Christiane Pfaff**[1,2] | **Tobias Wech**[1] (iD) | **Anne Slawig**[1,3] (iD) |
Gudrun Ruyters[4] | **Andrew Dewdney**[4] | **Ralf Ringler**[2] | **Herbert Köstler**[1] (iD)

[1]Department of Diagnostic and Interventional Radiology, University Hospital Würzburg, Würzburg, Germany

[2]X-Ray & Molecular Imaging Lab, Technical University Amberg-Weiden, Weiden, Germany

[3]Comprehensive Heart Failure Center Würzburg, Würzburg, Germany

[4]Siemens Healthcare, Erlangen, Germany

Correspondence
Manuel Stich, Department of Diagnostic and Interventional Radiology, University Hospital Würzburg, Oberdürrbacher Strasse 6, D-97080 Würzburg, Germany.
Email: e_stich_m@ukw.de

Funding information
Siemens Healthcare; Graduate School of Life Sciences - PhD Fellowship

Purpose: The gradient system transfer function (GSTF) characterizes the frequency transfer behavior of a dynamic gradient system and can be used to correct non-Cartesian k-space trajectories. This study analyzes the impact of the gradient coil temperature of a 3T scanner on the GSTF.

Methods: GSTF self- and B_0-cross-terms were acquired for a 3T Siemens scanner (Siemens Healthcare, Erlangen, Germany) using a phantom-based measurement technique. The GSTF terms were measured for various temperature states up to 45°C. The gradient coil temperatures were measured continuously utilizing 12 temperature sensors which are integrated by the vendor. Different modeling approaches were applied and compared.

Results: The self-terms depend linearly on temperature, whereas the B_0-cross-term does not. Effects induced by thermal variation are negligible for the phase response. The self-terms are best represented by a linear model including the three gradient coil sensors that showed the maximum temperature dependence for the three axes. The use of time derivatives of the temperature did not lead to an improvement of the model. The B_0-cross-terms can be modeled by a convolution model which considers coil-specific heat transportation.

Conclusion: The temperature dependency of the GSTF was analyzed for a 3T Siemens scanner. The self- and B_0-cross-terms can be modeled using a linear and convolution modeling approach based on the three main temperature sensor elements.

KEYWORDS
gradient impulse response function, gradient system response, gradient system transfer function, temperature dependency, thermal variation

---

1 | INTRODUCTION

It is commonly known that hardware imperfections of the MR scanner are caused by gradient coil coupling, amplifier imperfections, mechanical oscillations, and eddy currents, which give rise to gradient waveform infidelity.[1-6] These deviations between the actual and nominal gradients do not significantly influence the image quality in single-echo Cartesian imaging, because they mainly cause shifts of the entire k-space which are not visible in magnitude images. However, image artifacts have been shown for spiral[7-9] or for echo planar imaging (EPI) sequences.[7,8]

Besides the built-in eddy-current compensation and pre-emphasis techniques, which are integrated by the scanner vendors,[10-12] attempts have been made in the MR community to overcome those hardware imperfections by applying various strategies to compensate for gradient delays using postprocessing techniques.[13-16] Moreover, gradient field monitoring enables measuring the actual trajectories which are played out by the scanner using phantoms or field cameras.[7,8,17,18] Lately, this method was replaced by a more general technique which makes use of the linear and time-invariant system characteristics: the acquisition of the gradient system impulse response function (GIRF) or its Fourier transform, that is, the gradient system transfer function (GSTF).[19-21] The effect of different terms of the GSTF on image quality has been shown recently.[7,8,22] The GSTF information can be used for gradient correction, which can be applied for trajectory prediction[7,8] during image reconstruction or as a pre-emphasis[9,23] before the gradient waveform is played out by the scanner. Most beneficial, the GSTF can be acquired as a one-time calibration and can then be utilized to correct arbitrary gradient waveforms.[19] Consequently, this straightforward approach eliminates cumbersome and time-consuming trajectory measurement for each trajectory type, imaging protocol, or slice orientation.

An additional challenge arises when highly demanding applications may lead to heating of the MR system. Temperature changes could affect the gradient system response, which ultimately corrupts trajectory correction procedures.[24,25] Therefore, the aim of this study was to investigate the temperature dependency of the self- and B_0-cross-terms for a clinical 3T Siemens system and to compare different models for an accurate description of the temperature-dependent GSTF characteristics.

2 | METHODS

2.1 | GSTF theory

Assuming linear and time-invariant characteristics, the dynamic gradient system can be described by the GSTF. The GSTF specifies the frequency-dependent amplitude and phase transfer. This article only briefly presents the GSTF theory; a more detailed explanation is provided in the literature.[8,19,26,27]

The gradient response out(t) played out by the gradient system can be calculated (Equation 1) by convolving the nominal input gradient $g_{in}(t)$ with the GIRF h(t):

$$\text{out}(t) = g_{in}(t) * h(t) = \int_{-\infty}^{+\infty} g_{in}(\tau) \cdot h(t-\tau)\,d\tau. \quad (1)$$

In the frequency domain, this convolution can be described (Equation 2) as a simple multiplication of the respective Fourier-transformed quantities $G_{in}(f)$ and $H(f)$:

$$\text{Out}(f) = G_{in}(f) \cdot H(f). \quad (2)$$

In our implementation, the determination of $H(f)$ is performed by measuring the output as the response of N different triangular input gradients with different pulse widths. The measurement is performed using a standard spherical phantom. Determining the phase evolutions Φ_{slice1} and Φ_{slice2} in two parallel slices of distance Δx enables the calculation of the response out(t), which can be a gradient or B_0 output (Equations 3 and 4):

$$g_{out}(t) = \frac{1}{\Delta x \cdot \gamma} \cdot \frac{d}{dt} \left[\left(\Phi_{slice1}(t) - \Phi_{slice1,ref}(t) \right) \right. \\ \left. - \left(\Phi_{slice2}(t) - \Phi_{slice2,ref}(t) \right) \right], \quad (3)$$

$$B_{out}(t) = \frac{1}{2 \cdot \gamma} \cdot \frac{d}{dt} \left[\left(\Phi_{slice1}(t) - \Phi_{slice1,ref}(t) \right) \right. \\ \left. + \left(\Phi_{slice2}(t) - \Phi_{slice2,ref}(t) \right) \right]. \quad (4)$$

The reference phases $\Phi_{slice1,ref}(t)$ and $\Phi_{slice2,ref}(t)$ for both slices were additionally acquired by not playing out the triangular gradient waveforms. γ represents the gyromagnetic ratio. The gradient output $g_{out}(t)$ describes the response of the dynamic gradient system and the B_0 output the response of the B_0 field $B_{out}(t)$. Equations 3 and 4 assume that the slices are at equal distance $(\Delta x/2)$ of either side of the isocenter.

Finally, the transfer function can be calculated for every direction k, the input gradient is played out, and for every direction l the output gradient is measured (Equation 5):

$$H_{k,l}(f) = \frac{\sum_{i=1}^{i=N} G_{in_k}^{*\,i}(f) \cdot \text{Out}_{k,l}^i(f)}{\sum_{i=1}^{i=N} \left| G_{in_k}^i(f) \right|^2}, \quad \begin{array}{l} k = x, y, z \\ l = x, y, z, 0 \\ i = 1 \dots N \end{array} \quad (5)$$

The index i represents a particular triangular waveform. The self-term (first order) field components are represented by $k = l = [x, y, z]$ and the B_0-cross-term (0th order) field components for $k = [x, y, z]$ and $l = 0$.

2.2 | GSTF measurement and gradient heating

All experiments were performed on a 3T MAGNETOM Skyra MR scanner (Siemens Healthcare, Erlangen, Germany) with a bore diameter of 70 cm. Figure 1 shows the sequence diagram of the GSTF measurement and the heating sequence which was used in this study. The acquisitions of the self- and B_0-field-terms were achieved using a prototype sequence including 12 triangularly shaped input gradient pulses which lead to a broad spectral frequency coverage. The gradient pulse durations were varied between 100 and 320 μs with a fixed slew rate of 180 T/m/s. The signal phase was measured in two parallel slices, vertical to the input gradient direction with a slice position of ±16.5 mm from the isocenter and with a slice thickness of 3 mm. The flip angle was set to 90° and the bandwidth was 119 kHz for all acquisitions. Each readout had a duration of 10 ms. During gradient heating, 50 repetitions of the measurement were performed, while the cooling phase comprised 80 measurement repetitions. This results in heating periods of 40 minutes and cooling periods of 64 minutes. The maximum temperatures were reached at the end of each heating period. GSTF data were calculated for each repetition to achieve maximum temporal resolution.

The gradient temperature was monitored with 12 temperature sensors (TSs), integrated by the vendor. Three sensors are located on the gradient cable connectors and nine in the gradient coil. The temperature data were sampled with a temporal resolution of 10 seconds. To achieve different system temperatures, the GSTF measurement sequence was supplemented by bipolar trapezoidal heating gradients, which can be enabled for every gradient axis. All heating experiments were performed with heating gradients of constant amplitude (A_H = 23 mT/m) and variable duration (t_H = 120–480 ms) at a constant repetition time of 1 second. This means that the duty cycles for the heating gradients were varied between 12% and 48%. These parameters generate gradient system local temperatures of up to 45°C.

2.3 | Temperature-dependent GSTF models

A linear model was used to describe the temperature-dependent changes $\Delta\mathbf{GSTF}_{self}$ of the transfer function in the self-terms (Equation 6):

$$\Delta\mathbf{GSTF}_{self} = \mathbf{I}_{meas} \cdot \mathbf{m}, \qquad (6)$$

with the measured input $\mathbf{I}_{meas}$ and model parameter $\mathbf{m}$.

Two different approaches were implemented. The first one only considers the measured temperature values T as the model input $\mathbf{I}_{meas}$ (Equation 7):

$$\mathbf{I}_{meas} = \begin{pmatrix} 1 & T(TS1)_{t=0} & \cdots & T(TS12)_{t=0} \\ \vdots & \vdots & \ddots & \vdots \\ 1 & T(TS1)_{t=N} & \cdots & T(TS12)_{t=N} \end{pmatrix}. \qquad (7)$$

As shown in Equation 7, the measured input consists of the temperatures T for up to 12 TSs. The temperature values were acquired for discrete time points from t = 0 to t = N.

Besides the sensor temperatures T, the second approach also includes the temperature derivatives $\dot{T}$ for the measured input $\mathbf{I}_{meas}$.

Additionally, Equation 6 was evaluated for two different sensor combination approaches: First, a real-sensor model (RSM) only containing gradient coil sensors GS 3, 4, and 9, which show the strongest temperature response for x/y/z-axis gradient. Second, a virtual-sensor model (VSM) was created, where the measured input $\mathbf{I}_{meas}$ consists of 1 to 12 virtual sensors resulting from a principal component analysis (PCA) for all 12 sensors.

To describe the temperature-dependent changes of the B_0-cross-terms, a linear model (RSM-based, gradient coil sensors GS 3, 4, and 9) was used with and without including gradient cable sensors (CS). These linear approaches were compared to a convolution-model approach, where Bateman-functions $\mathbf{b}(t)$ were used as convolution kernels (Equation 8):

FIGURE 1 GSTF measurement sequence using N = 12 triangular shaped pulses. The trapezoidal bipolar gradient pulses, which heat the gradient system to a steady temperature state. The temperature can be adjusted by the gradient amplitude A_H and the gradient duration t_H. ADC = analog to digital converter; RF = radiofrequency
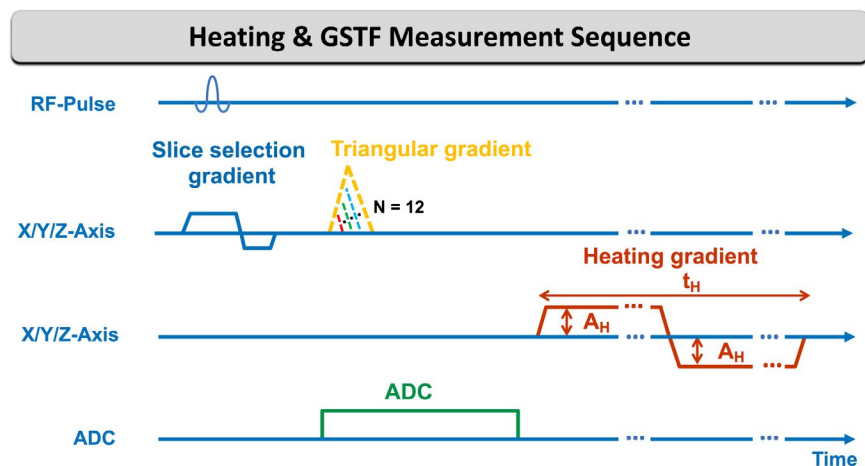
$$\Delta \mathbf{GSTF}_{B0} = (\mathbf{I}_{meas} * \mathbf{b}(t)) \cdot \mathbf{m}. \qquad (8)$$

The Bateman-convolution kernels were defined as $b(t) = e^{-k_1 \cdot t} - e^{-k_2 \cdot t}$. For Equation 8, two different model representations were compared: The same convolution kernel is applied to every sensor (one convolution model; OCM), or sensor-specific kernels are used (individual convolution model; ICM). The model parameters m, k_1, and k_2 were fitted for all approaches using least-square minimization.

All different modeling approaches were compared quantitatively using χ^2 between 0 and 4 kHz as a goodness-of-fit measure. The Bayesian information criterion (BIC) was calculated to compare models with different numbers of independent parameters. ΔBIC values can be used to rank the model performance.

3 | RESULTS

3.1 | Temperature characteristics of the self- and B_0-cross-terms

Figure 2A shows the determined temperature curves for different duty cycles of the heating sequence: 0% (cooling), 12%, 24%, 36%, and 48%. The higher the duty cycle of the heating sequence, the higher the maximum temperature reached at the end of the heating period. Coil sensor 9 showed the
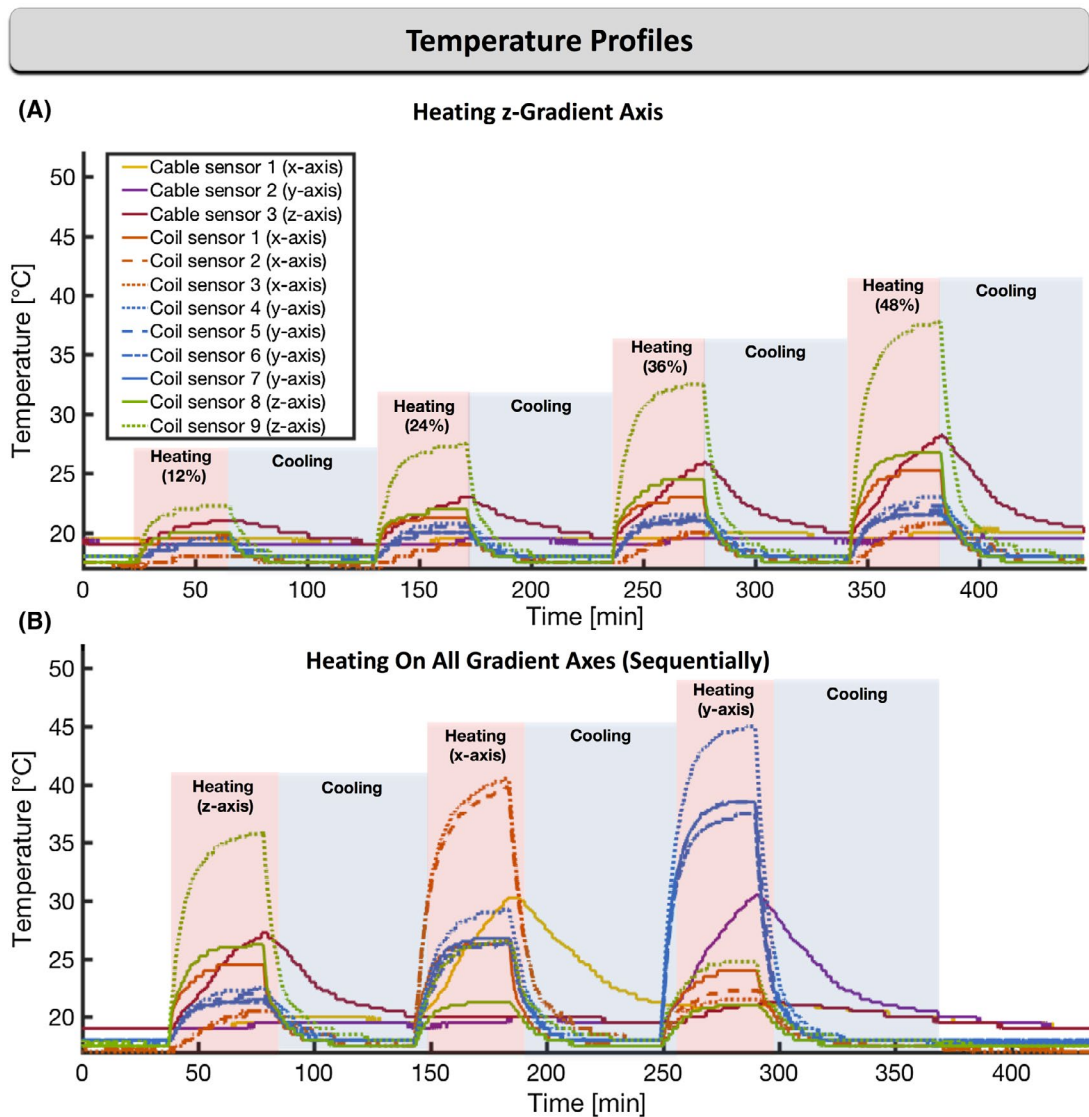
FIGURE 2 Temperature data are logged every 10 seconds by 12 temperature sensors, during heating experiments. Each heating cycle (red sectors) is followed by a cooling period (blue sectors). The gradient coil temperature sensors with the highest sensitivity on every gradient axis are coil sensors 3, 4, and 9, and the sensors mounted at the gradient cable connectors are represented with dash-point lines (cable sensors 1–3). Temperature profile (A) shows different thermal levels on the z-gradient axis, which were accomplished by varying the heating duty cycle between 12% and 48%. This results in 22°C, 27°C, 32°C, and 37°C for coil sensor 9 at the end of each heating period, respectively. Temperature profile (B) visualizes heating of the x-, y-, and z-gradient axes, when the same heating duty cycle of 48% is applied
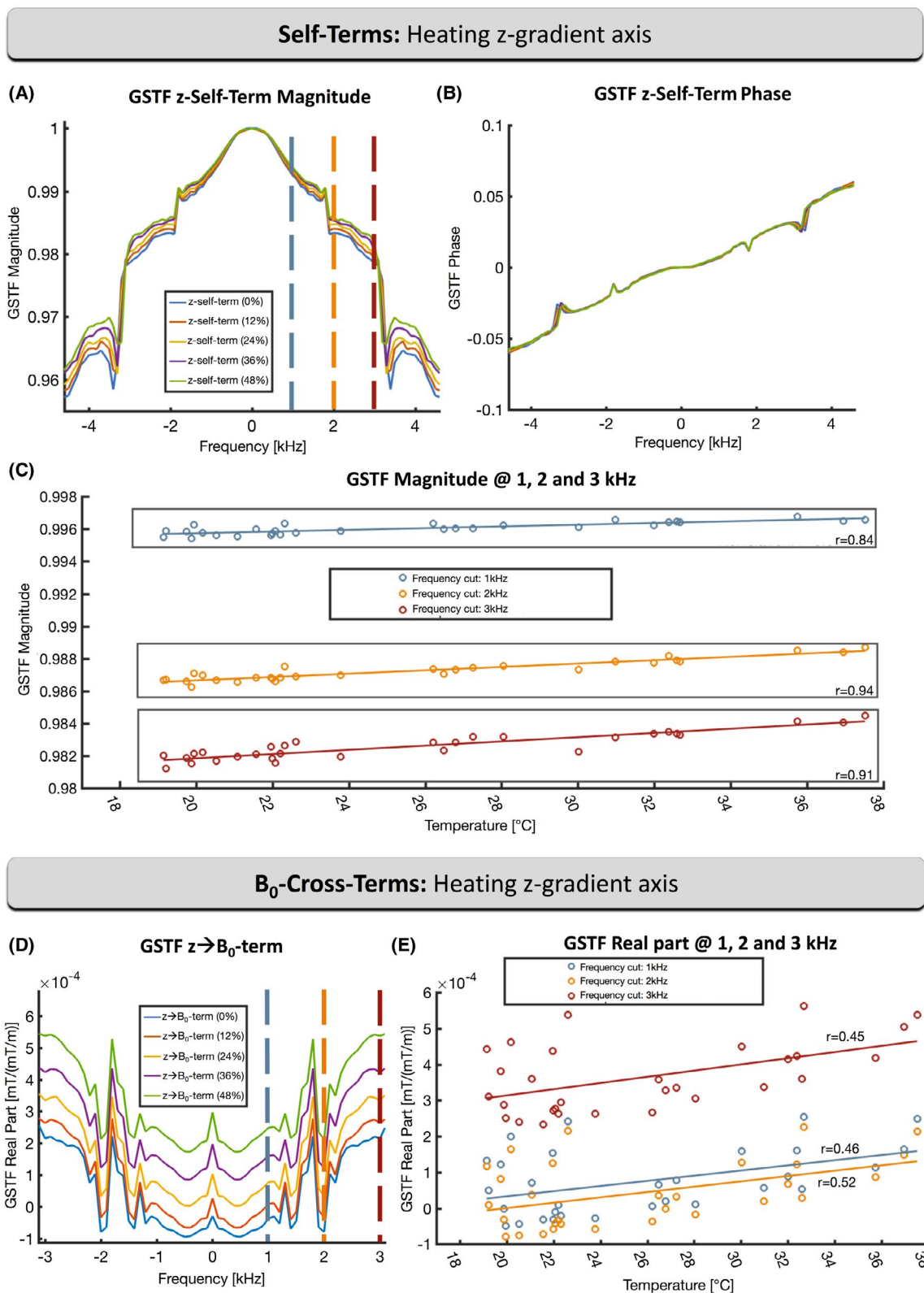
FIGURE 3 The z-self term increases linearly with rising temperatures (A), whereas the phase response is mostly independent, apart for tiny deviations (<0.02) for the mechanical resonances (B). The linear temperature dependency is visualized exemplarily for three frequencies at 1, 2, and 3 kHz (dashed lines in (A)), exhibiting high correlation coefficients r > 0.84 (C). The temperature dependency for the z→B_0 term is visualized in (D). There is no linear temperature dependency r < 0.51 for the z→B_0 term, which is exemplarily shown for the frequencies at 1, 2, and 3 kHz (E). (A), (B), and (D) show data of the end of a cooling or heating period for different duty cycles (0%, 12%, 24%, 36%, and 48%). Temperatures in (C) and (E) are values at the end of the heating periods measured by coil sensor 9. Temperature and GSTF values are averaged over 8 minutes

following maximum temperatures at the end of the heating phases: 22.3°C (duty cycle 12%), 27.5°C (duty cycle 24%), 32.5°C (duty cycle 36%), and 37.8°C (duty cycle 48%). At the end of each cooling phase, the standard reference temperature (~18°C) was reestablished again. The corresponding z-self-term data at different duty cycles is visualized in Figure 3A. The GSTF magnitude responses show a considerable temperature dependency, mainly a broadening of magnitude profiles and a slight shift of the mechanical resonances toward lower frequencies for higher temperatures. Conversely, the temperature-dependent deviation in the phase is negligible (Figure 3B); at most, the mechanical resonances are slightly affected by temperature changes (Figure 3B). Figure 3C displays the GSTF at three frequencies at 1, 2, and 3 kHz of the z-self-term and shows that the magnitude is linearly dependent on the temperature (correlation, $r > 84\%$).

For the $z \rightarrow B_0$-term, the change in the magnitude is visualized in Figure 3D. The GSTF at frequencies at 1, 2, and 3 kHz indicate that magnitude and temperature do not correlate well ($r < 0.51$; Figure 3E).

3.2 | Temperature-dependent self- and B_0-cross-term models

All model approaches were created based on the temperature profile, visualized in Figure 2B. Here, the heating gradient was used to heat all three gradient axes sequentially with a fixed duty cycle of 48%, which leads to maximum temperatures of 36.0°C (coil sensor 9) for the z-axis, 40.5°C (coil sensor 3) for the x-axis, and 45.0°C (coil sensor 4) for the y-axis. Cable sensors show a slower response behavior than gradient coil sensors.

The PCA analysis of the VSM-dependent self-terms shows that at least the first three main sensor components are required to model the measured GSTF magnitude curve. The sum of the first three eigenvalues of the measured input I_{meas} cover
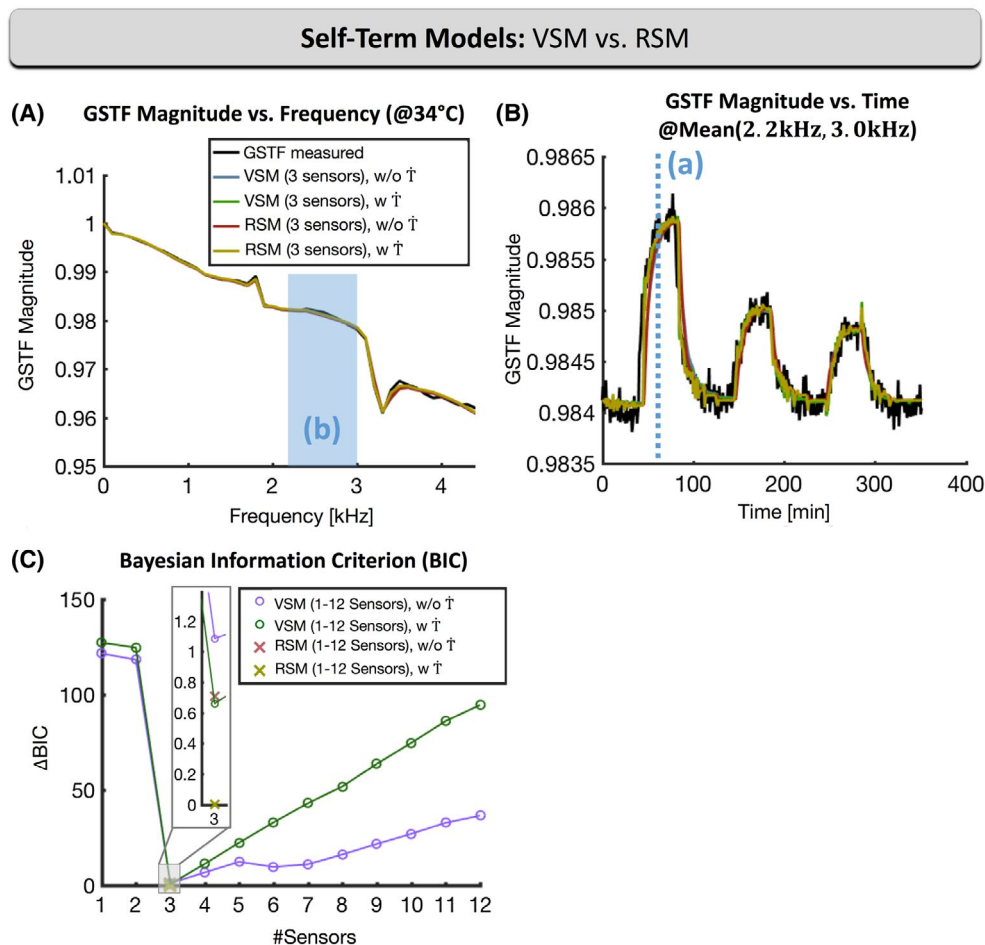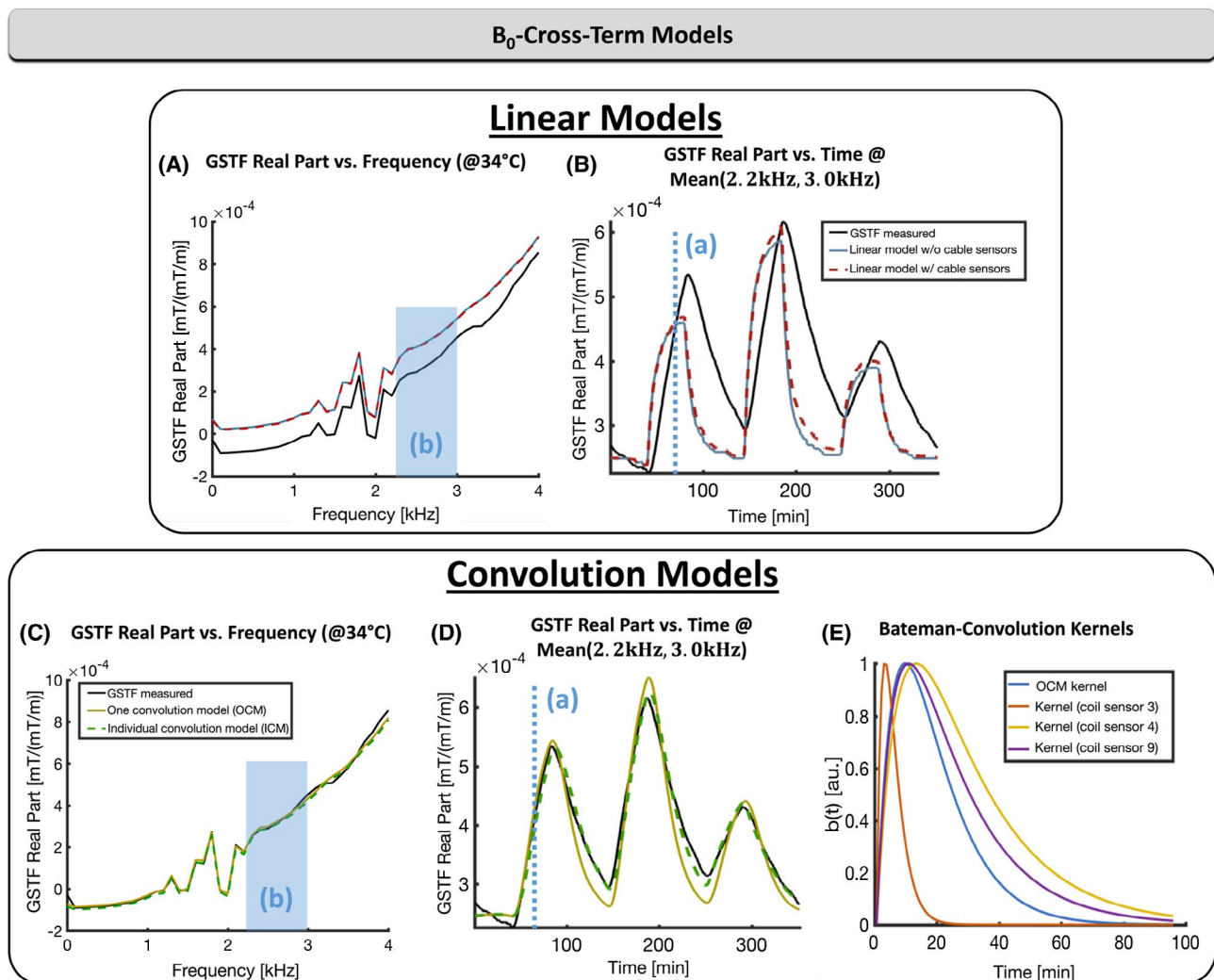

FIGURE 4 (A) Comparison of the measured z-self-term magnitude at 34°C and the prediction of different model approaches: VSM (three sensors) and RSM (three sensors), with/without temperature derivative (Ṫ). (B) Temporal comparison of the z-self-term magnitude (average of frequency range) according to the heating profile (Figure 2B). (C) Small ΔBIC values suggest that the use of 3 sensors in a linear model provides the best predication of the measured data and are most suitable for the linear model. An integration of temperature derivatives is not necessary (ΔBIC < 2)

with 97% most of the contained information. The self-term GSTF in the frequency domain (for 34°C, at coil sensor 9) and the temporal profile (magnitude averaged for 0–5 kHz) show a good qualitative fit with and without including temperature derivatives (Figure 4A,B). The RSM is based on the gradient coil sensors 3, 4, and 9, with the highest temperature response for each gradient axis. The deviations between measured and modeled data are also small for the RSM (Figure 4A,B). The χ^2 values are <0.0012 for all modeling approaches and only show small differences in the region of mechanical resonances. The ΔBIC values in Figure 4C reveal that the most suitable models are using three sensors. Including more sensors increases BIC values. The differences in ΔBIC (<2) of the different model approaches using three sensors are too small to favor one model.

In contrast to the self-terms, the B_0-cross-terms are not described well by a linear model (Figures 3E and 5A,B). The

differences between the B_0-cross-terms and the linear fit are systematic and cannot be explained by the noise level. Also adding three cable sensors to the linear RSM, which are characterized by a more temperature-preserving behavior (Figure 2), does not have a major impact. Contrary to the linear models, convolution models are a good representation of the temperature-dependent changes of the B_0-field-term. The OCM delivers good modeling results, which can be even surpassed by the ICM (Figures 5C, D), which considers sensor-specific heat transportation instead of assuming the same heat transportation model for all sensors. The Bateman convolution kernels for both approaches are visualized in Figure 5E. The modeling results can also be expressed quantitatively by the corresponding χ^2 values, which are lower for the Bateman approaches than for the linear approaches. The smallest χ^2 values were achieved using the ICM ($\chi^2 < 0.0012$). The ΔBIC values support this statement: The ICM fits the

FIGURE 5 Comparison of the measured z→B_0-cross-term at 34°C and the predication of linear model approaches with/without cable sensors (A) and the convolution models (C). Panels (B, D) show the corresponding temporal comparison of the z→B_0-cross-term according to the heating profile (Figure 2B). Panels (A-D) visualize that the convolution models deliver much better fitting results than the standard linear model, which shows only a small improvement by including the cable sensors. Panel (E) displays the corresponding Bateman convolution kernels for the OCM and ICM

B_0-cross-terms best ($\Delta BIC = 0$), followed by the OCM as the second best model ($\Delta BIC = 345$). $\Delta BIC = 1125$ and $\Delta BIC = 1172$ were obtained for the linear model with and without cable sensors, respectively.

4 | DISCUSSION AND CONCLUSION

In this work, the temperature dependency of the gradient system transfer function was analyzed for the self- and B_0-cross-terms. All temperature experiments were performed on a 3T Siemens scanner system, using temperature sensors, which are integrated by the vendor, for precise monitoring of the temperature of a high temporal resolution.

The GSTF was acquired with a phantom-based thin slice approach.[8] Acquisition parameters, like the slice distance and thickness, were used as described by Campbell-Washburn et al.[8] The read-out duration was set to 10 ms, which results in a frequency resolution of 100 Hz.

We observed that there is a linear relationship between the temperature-induced magnitude change and the gradient temperature for the self-term magnitude response, whereas the phase response showed only minor temperature-induced deviations. We observed slight shifts of the mechanical resonances toward lower frequencies for the self-terms (Figure 3) during gradient heating. The B_0-cross-terms also indicated changes when heating the gradient system. A linear relationship between the change in the B_0-cross-term and the temperature was not evident in this case.

This study further shows that a linear model is eligible for modeling the GSTF self-terms. For both temperature experiments, where only one gradient axis (Figure 2A) and all 3 gradient axes (Figure 2B) were heated, three sensors are necessary and sufficient to describe the system comprehensively. Using more than three sensors resulted in an increased BIC. The RSM shows that the sensor with the highest temperature contribution for each gradient axis is a meaningful choice for describing the GSTF course adequately. Moreover, it is not necessary to include the temperature derivatives in the model approach. For the B_0-cross-terms, heat transportation has to be considered to describe the temperature response characteristics. Therefore, a Bateman-convolution kernel was introduced to consider heat transportation in the model. The best result could be achieved for the ICM with three sensor-specific Bateman-convolution kernels, which describe individual heat transportation for every gradient axis. We assume the slow B_0 effect must be traced back to heating of other parts of the scanner rather than the gradient coils. Possible candidates might be shim plates or gradient wires.

Busch et al.[25] also measured the GSTF self-terms for different temperatures and noticed changes in the magnitude response while heating a 3T Achieva scanner (Philips Healthcare, Best, The Netherlands). As reported in this work, no variations in gradient delays were detected[25] for different temperature states. Similar to our results, some temperature-dependent shifts of the mechanical resonances could be observed. The analysis of the effect of these shifts for different applications will be considered in future work. In contrast to that, Brodsky et al.[24] reported changes in the gradient delay times after applying gradient heating for a 1.5T Excite scanner (GE Healthcare, Waukesha, WI). Previous studies[28,29] also worked on the analysis and model generation for the gradient system transfer functions of Philips systems. In contrast to the analysis presented here, temperature sensor elements were manually attached at several scanner locations. In these studies,[28,29] the thermal model of the GIRF was created using seven temperatures and their time derivatives combined with a linear modeling approach. The researchers' observation, that the integration of temperature derivatives is beneficial, might be reasoned by the fact that the sensors are not directly integrated within the coils as it is the case in this work. In our study, the most efficient model was obtained without including temperature derivatives and by using only the three most sensitive built-in temperature sensors. To model the B_0-cross-terms, the introduction of additional convolution kernels was necessary to mimic heat transportation.

Besides a global frequency-dependent B_0-shift attributable to gradient heating, Hermann et al.[30] also reported on B_0 variations in a spatial dependency after heating the gradient system with a periodically rotated overlapping parallel lines with enhanced reconstruction EPI diffusion tensor imaging (DTI) sequence. Our focus laid on the dynamic properties of the gradient system and the static effects as described in Hermann et al.[30] were not investigated in this work.

In conclusion, this work successfully analyzed the temperature dependency of the GSTF self- and B_0-cross-terms and developed models to predict authentic gradient system characteristic for arbitrary temperature states. In the future, this knowledge can be integrated into GSTF-based trajectory correction techniques[7-9,22] by correcting the nominal gradient waveforms with the GSTF which fits the current temperature sate of the gradient system. This could further diminish artefacts, especially in warm temperature states which can be obtained by demanding sequences, as for example in DTI.

CONFLICT OF INTEREST

ORCID

Manuel Stich https://orcid.org/0000-0002-0429-4419
Tobias Wech https://orcid.org/0000-0002-2813-7100
Anne Slawig https://orcid.org/0000-0003-1412-244X
Herbert Köstler https://orcid.org/0000-0001-6207-9226

REFERENCES

1. Wu YH, Chronik BA, Bowen C, Mechefske CK, Rutt BK. Gradient induced acoustic and magnetic field fluctuations in a 4 T whole-body MR imager. *Magn Reson Med*. 2000;44:532–536.
2. Clayton DB, Elliott MA, Leigh JS, Lenkinski RE. 1H Spectroscopy without solvent suppression: characterization of signal modulations at short echo times. *J Magn Reson*. 2001;153:203–209.
3. Foerster BU, Tomasi D, Caparelli EC. Magnetic field shift due to mechanical vibration in functional magnetic resonance imaging. *Magn Reson Med*. 2005;54:1261–1267.
4. Jehenson P, Westphal M, Schuff N. Analytical method for the compensation of eddy-current effects induced by pulsed magnetic field gradients in NMR systems. *J Magn Reson*. 1990;90:264–278.
5. Van Vaals JJ, Bergman AH. Optimization of eddy-current compensation. *J Magn Reson*. 1990;90:52–70.
6. Wysong RE, Madio DP, Lowe IJ. A novel eddy current compensation scheme for pulsed gradient systems. *Magn Reson Med*. 1994;31:572–575.
7. Vannesjo SJ, Graedel NN, Kasper L, et al. Image reconstruction using a gradient impulse response model for trajectory prediction. *Magn Reson Med*. 2016;76:45–58.
8. Campbell-Washburn AE, Xue H, Lederman RJ, Faranesh AZ, Hansen MS. Real-time distortion correction of spiral and echo planar images using the gradient system impulse response function. *Magn Reson Med*. 2016;75:2278–2285.
9. Stich M, Wech T, Slawig A, et al. Gradient waveform pre-emphasis based on the gradient system transfer function. *Magn Reson Med*. 2018;80:1521–1532.
10. Jehenson P, Westphal M, Schuff N. Analytical method for the compensation of eddy-current effects induced by pulsed magnetic field gradients in NMR systems. *J Magn Reson*. 1990;90:264–278.
11. Zur Y, Stokar S. An algorithm for eddy currents symmetrization and compensation. *Magn Reson Med*. 1996;35:252–260.
12. Bieri O, Markl M, Scheffler K. Analysis and compensation of eddy currents in balanced SSFP. *Magn Reson Med*. 2005;54:129–137.
13. Tan H, Meyer CH. Estimation of k-space trajectories in spiral MRI. *Magn Reson Med*. 2009;61:1396–1404.
14. Block K, Ücker M. Simple method for adaptive gradient-delay compensation in radial MRI. In Proceedings of the 19th Annual Meeting of ISMRM, Montréal, Canada, 2011. p. 2816.
15. Peters DC, Korosec FR, Grist TM, et al. Undersampled projection reconstruction applied to MR angiography. *Magn Reson Med*. 2000;45:91–101.
16. Wech T, Tran-Gia J, Bley TA, Köstler H. Using self-consistency for an iterative trajectory adjustment (SCITA). *Magn Reson Med*. 2015;73:1151–1157.
17. Duyn JH, Yang Y, Frank JA, van der Veen JW. Simple correction method for k-space trajectory deviations in MRI. *J Magn Reson*. 1998;132:150–153.
18. Zhang Y, Hetherington HP, Stokely EM, Mason GF, Twieg DB. A novel k-space trajectory measurement technique. *Magn Reson Med*. 1998;39:999–1004.
19. Vannesjo SJ, Haeberlin M, Kasper L, et al. Gradient system characterization by impulse response measurements with a dynamic field camera. *Magn Reson Med*. 2013;69:583–593.
20. Liu H, Matson GB. Accurate measurement of magnetic resonance imaging gradient characteristics. *Materials (Basel)*. 2014;7:1–15.
21. Addy NO, Wu HH, Nishimura DG. Simple method for MR gradient system characterization and k-space trajectory estimation. *Magn Reson Med*. 2012;68:120–129.
22. Robison RK, Li Z, Wang D, et al. Correction of B0 eddy current effects in spiral MRI. *Magn Reson Med*. 2018;81:2501–2513.
23. Goora FG, Colpitts BG, Balcom BJ. Arbitrary magnetic field gradient waveform correction using an impulse response based pre-equalization technique. *J Mag Reson*. 2014;238:70–76.
24. Brodsky EK, Samsonov AA, Block WF. Characterizing and correcting gradient errors in non-cartesian imaging: Are gradient errors linear time-invariant (LTI)? *Magn Reson Med*. 2009;62:1466–1476.
25. Busch J, Vannesjo SJ, Barmet C, Pruessmann KP, Kozerke S. Analysis of temperature dependence of background phase errors in phase-contrast cardiovascular magnetic resonance. *J Cardiovasc Magn Reson*. 2014;16:97.
26. Stich M, Wech T, Slawig A, et al. B0-component determination of the gradient system transfer function using standard MR scanner hardware. In Proceedings of the Joint Annual Meeting of ISMRM-ESMRMB, Paris, France, 2018. p. 0942.
27. Brodsky EK, Klaers JL, Samsonov AA, et al. Rapid measurement and correction of phase errors from B0 eddy currents: impact on image quality for non-Cartesian imaging. *Magn Reson Med*. 2013;69:509–515.
28. Dietrich BE, Nussbaum J, Wilm BJ, et al. Thermal variation and temperature-based prediction of gradient response. In Proceedings of the 25th Annual Meeting of ISMRM, Honolulu, HI, 2017. p. 0079.
29. Nussbaum J, Wilm BJ, Dietrich BE, et al. Improved thermal modelling and prediction of gradient response using sensor placement guided by infrared photography. In Proceedings of the Joint Annual Meeting of ISMRM-ESMRMB, Paris, France, 2018. p. 4210.
30. Hermann KH, Krämer M, Reichenbach JR. Global and spatially varying B0 drifts due to gradient system heating. In Proceedings of the 21st Annual Meeting of the ISMRM, Melbourne, Australia, 2012. p. 2411.